Observability of forming planets and their circumplanetary discs II. – SEDs and near-infrared fluxes

Szulágyi, J ; Dullemond, C P ; Pohl, A ; Quanz, S P

Abstract: Detection of forming planets means detection of the circumplanetary disc (CPD) in reality, since the planet is still surrounded by a disc at this evolutionary stage. Yet, no comprehensive CPD modelling was done in near-infrared (near-IR) wavelengths, where high contrast imaging is a powerful tool to detect these objects. We combined 3D radiative hydrodynamic simulations of various embedded planets with radmc-3d radiative transfer post-processing that includes scattering of photons on dust particles. We made synthetic images for Very Large Telescope NaCo/ERIS in the Ks, L , and M bands as well as examined the spectral energy distributions (SEDs) of discs between 1 m and 10 cm. We found that the observed magnitudes from the planet's vicinity will mostly depend on the CPD parameters, not on the planet's. The CPD is 20–100x brighter than the embedded planet in near-IR. We also show how the CPD parameters, e.g. the dust-to-gas ratio will affect the resulting CPD magnitudes. According to the SEDs, the best contrast ratio between the CPD and circumstellar discs is in sub-mm/radio wavelengths and between 8–33 m in case if the planet opened a resolvable, deep gap (5MJup), while the contrast is particularly poor in the near-IR. Hence, to detect the forming planet and its CPD, the best chance today is targeting the sub-mm/radio wavelengths and the 10- m silicate feature vicinity. In order to estimate the forming planet's mass from the observed brightness, it is necessary to run system specific disc modelling.

DOI: https://doi.org/10.1093/mnras/stz1326

Monthly Notices
of the
ROYAL ASTRONOMICAL SOCIETY

MNRAS **487,** 1248–1258 (2019)
Advance Access publication 2019 May 16

doi:10.1093/mnras/stz1326

Observability of forming planets and their circumplanetary discs II. – SEDs and near-infrared fluxes

J. Szulágyi [1]★ C. P. Dullemond,[2] A. Pohl[2,3] and S. P. Quanz[4]

[1]*Center for Theoretical Astrophysics and Cosmology, Institute for Computational Science, University of Zürich, Winterthurerstrasse 190, CH-8057 Zürich, Switzerland*
[2]*Heidelberg University, Center for Astronomy, Institute of Theoretical Astrophysics, Albert-Ueberle-Str. 2, D-69120 Heidelberg, Germany*
[3]*Max-Planck-Institute for Astronomy, Königstuhl 17, D-69117 Heidelberg, Germany*
[4]*ETH Zürich, Institute for Particle Physics and Astrophysics, Wolfgang-Pauli-Strasse 27, CH-8093, Zürich, Switzerland*

Accepted 2019 May 9. Received 2019 May 9; in original form 2018 October 24

ABSTRACT

Detection of forming planets means detection of the circumplanetary disc (CPD) in reality, since the planet is still surrounded by a disc at this evolutionary stage. Yet, no comprehensive CPD modelling was done in near-infrared (near-IR) wavelengths, where high contrast imaging is a powerful tool to detect these objects. We combined 3D radiative hydrodynamic simulations of various embedded planets with RADMC-3D radiative transfer post-processing that includes scattering of photons on dust particles. We made synthetic images for Very Large Telescope NaCo/ERIS in the *Ks*, L', and M' bands as well as examined the spectral energy distributions (SEDs) of discs between 1 μm and 10 cm. We found that the observed magnitudes from the planet's vicinity will mostly depend on the CPD parameters, not on the planet's. The CPD is 20–100x brighter than the embedded planet in near-IR. We also show how the CPD parameters, e.g. the dust-to-gas ratio will affect the resulting CPD magnitudes. According to the SEDs, the best contrast ratio between the CPD and circumstellar discs is in sub-mm/radio wavelengths and between 8–33 μm in case if the planet opened a resolvable, deep gap ($\geq 5 M_{\rm Jup}$), while the contrast is particularly poor in the near-IR. Hence, to detect the forming planet and its CPD, the best chance today is targeting the sub-mm/radio wavelengths and the 10-μm silicate feature vicinity. In order to estimate the forming planet's mass from the observed brightness, it is necessary to run system specific disc modelling.

Key words: radiative transfer – planets and satellites: detection – planets and satellites: formation – protoplanetary discs – infrared: planetary systems.

1 INTRODUCTION

The observations of forming planets are the keys to understand the giant planet formation processes. For this purpose, high-contrast imaging is often used, mainly in the near-infrared (near-IR). This way hot, point-like sources can be detected within the natal circumstellar disc (CSD), for which a natural, possible explanation is a protoplanet. There are a handful of such detections, the most obvious example being the recent discovery of PDS 70b (Keppler et al. 2018). Furthermore, there is one candidate around MWC 758 (Reggiani et al. 2017), three candidates around LkCa15 (Kraus & Ireland 2012; Sallum et al. 2015), two potential forming planets around HD100546 (Brittain et al. 2014; Quanz et al. 2015; Currie et al. 2014), two around HD169142 (Reggiani et al. 2014; Osorio et al. 2014), even though the origins of these hot spots are in some cases debated, as they could also be CSD features (Follette et al. 2017; Rameau et al. 2017).

While there is still ongoing gas accretion to the forming giant planet, it is surrounded by its own disc, the so-called circumplanetary disc (CPD; e.g. Quillen & Trilling 1998; Lubow, Seibert & Artymowicz 1999; Kley 1999; Lubow & D'Angelo 2006; Ayliffe & Bate 2009, 2012. Roughly speaking, the lifetime of the gaseous CPD is nearly equal to the gaseous CSD lifetime, because the CPD is constantly fed from the natal protoplanetary disc (Szulágyi et al. 2014; Szulágyi 2017). As the gaseous CSD is dissipating, the transport of matter on to the CPD also ceases, the two discs surface density evolves together (Szulágyi 2017). When there is no more gas left in the CSD near the location (the feeding zone) of the planet and CPD, the feeding stops. As the CPD mass is very small even during the class II phase of the CSD ($\sim 10^{-3} M_{\rm planet}$, Szulágyi 2017), at the time when the CSD disappears, the CPD is even lighter.

★ E-mail: judit.szulagyi@uzh.ch

This small mass ($<10^{-3}M_{planet}$) will quickly disappear, partially by being accreted on to the gas giant, and by being dissipated by other processes (e.g. viscous spreading). Therefore, detecting a forming planet is actually detecting its gaseous CPD.

There is no comprehensive study made to date about detecting CPDs in the near-IR. Quillen & Trilling (1998) performed analytical calculations which revealed that the CPD should be bright in the near–mid-IR. Brunngräber & Wolf (2018) did a parameter study using solely a radiative transfer (RT) algorithm to understand whether hotspots of protoplanets can be detected in the mid-IR with the upcoming VLTI/MATISSE instrument. This study however did not include CPD, given there were no hydrodynamic simulations made. Borra & Deschatelets (2018) have investigated the detection of planetary signal by reflected light of the host star using autocorrelation of spectra. Eisner (2015) has studied the SEDs of potential CPDs by downscaling the stellar spectrum to a colder blackbody. Zhu (2015) computed the disc spectrum via the emission from the atmosphere of a viscous, geometrically thin, optically thick accretion disc with a constant mass accretion rate. Due to the large debate in the community about whether the detected hotspots are real planets or disc features, here we address the observability of CPDs in the near-IR. We also provide their spectral energy distribution (SED) between 1 μm and 10 cm. We did a thorough study including temperature-included (i.e. radiative) 3D gas hydrodynamic simulations that were post-processed with a wavelength-dependent RT algorithm that includes scattering on dust particles. Finally, we convolved the synthetic images with a Gaussian kernel to mimic observational data, using a point spread function (PSF) for VLT (Very Large Telescope)/NaCo and VLT/ERIS. Because the brightness strongly depends on the opacity, we carefully made an opacity table that was consistently used both in the hydrodynamic simulations and in the post-processing RT runs. Our simulations include a CSD with an embedded planet at 50 au. Between the different runs, we changed the mass of the planet between Saturn, Jupiter, 5-Jupiter, and 10-Jupiter mass. These runs were made with the same surface density and same viscosity, because a full parameter space cannot be explored with these computationally expensive simulations.

In the first paper of this series, we looked at the CPD observability at sub-mm/radio wavelength (Szulágyi et al. 2018), and in next one we plan to address the scattered light imaging with polarization for instruments like VLT/SPHERE.

2 METHODS

As a first step we carried out radiative hydrodynamic simulations of the protoplanetary disc with a forming planet embedded within (Section 2.1). Then, we used the RADMC-3D RT tool to create wavelength-dependent images of the systems, including photon scattering on the dust particles (Section 2.2). Finally, we convolved the images with a diffraction limited PSF for the VLT/NaCo and VLT/ERIS instruments (Davies et al. 2018; Section 2.3) and calculated the apparent magnitudes of the CPDs and of the embedded planets from these images. We also created SEDs between 1 μm and 10 cm to understand which wavelength range is the best to detect the CPDs.

2.1 Hydrodynamic simulations

We performed 3D radiative hydrodynamic simulations of CSDs that have forming planets embedded in them with various planetary masses. The orbital distance of the planets from their star were 50 au. We used the JUPITER code, that was developed by Masset and Szulágyi (de Val-Borro et al. 2006; Szulágyi et al. 2014, 2016a) that not only solves Euler equations but also RT in the flux-limited diffusion approximation with the two-temperature approach (e.g. Commerçon et al. 2011; Bitsch et al. 2014) that calculates the temperature field for the gas. The gas can heat up due to adiabatic compression, viscous heating, and stellar irradiation, while it can cool through adiabatic expansion and radiative diffusion. The vicinity of the gas giant is heated up mainly by the accretion process (Szulágyi et al. 2016a), as the gas tries to fall on to the planet, leading to adiabatic compression in this region. In a fast rotating (i.e. cold) CPD, the viscous heating is also playing a role. The stellar irradiation, however, has no effect in the circumplanetary area. It only heats the atmosphere of the CSD, as the CPD is shielded from the stellar photons by the inner CSD. For observational predictions in the optical and near-IR, it is very important to simulate the CSD atmosphere (i.e. optically thin) regions, because here the photons can scatter multiple times before they get absorbed.

The Rosseland- and Planck-mean opacities used in the radiation-hydrodynamics code are constructed self-consistently from frequency-dependent dust opacities computed with a version of the MIE code from Bohren & Huffman (1984). The dust consists of 40 per cent silicates, 40 per cent water, and 20 per cent carbonaceous material (Draine 2003; Zubko et al. 1996; Warren & Brandt 2008), assuming micrometre-sized, spherical and compact grains. The dust-to-gas ratio was set to 1 per cent, constant everywhere inside the simulation. The opacity table accounts for the evaporation of the various dust species. We set the evaporation temperature for water, silicate, and carbon to 170, 1500, and 2000 K, respectively. Therefore, above 2000 K the gas opacities play a role, that were taken from Bell & Lin (1994). We connected the different opacity regimes with splines to ensure smooth transitions. The hydrodynamic code uses Rosseland-mean opacities, more precisely the mass-weighted averages of the three dust species. In each cell of the hydrodynamic simulation, the code uses the density and temperature of the given cell to look up what value of opacity it should use there. Then, the flux-limited diffusion approximation algorithm finds the new temperature of the cell via an iterative method. In conclusion, even though the dust is not treated explicitly in the gas hydrodynamic simulation as a secondary fluid, its effect on the temperature of the disc is taken into account through the dust opacities (with the limit of assuming a constant dust-to-gas ratio of 1 per cent).

The star was assumed to have solar properties in the simulations and in the opacity table. Given that we were particularly interested in the planet's vicinity – where high resolution is necessary to get the temperatures correctly, we used mesh refinement in this region. This means that while the ring of the CSD has been simulated with a lower resolution (680 cells azimuthally over 2π, 215 cells radially between 20 and 120 au, and 20 cells in the colatitude direction over 7.4 deg opening angle from the mid-plane), the Hill sphere of the planet is well resolved with four levels of refinement for these planetary masses and orbital separations. Each refinement doubles the resolution in each spatial direction, so the final resolution in the planet vicinity was approximately 0.029 au. Even though in a usual CSD there is still some gas left within 20 au from the star, this region has no effect on the CPD, that is located at 50 au from the star, hence we did not simulate this inner CSD region to save computational time.

The CSD ring had a mass of $\sim 10^{-2}\,M_{Sun}$ with a surface density slope of -0.5 initially, which evolved due to the heating–

cooling effects and the inclusion of the planets (i.e. gap-opening). We performed four different simulations with different planetary masses: a Saturn-mass gas giant, a Jupiter, a 5 M_{Jup}, and a 10 M_{Jup} gas giant. The final planet masses were reached over 50 orbits through a smooth, sinusoidal function, to not perturb the gas flow very abruptly. Once this initial growth phase was over, the planet masses were kept fixed and the results were evaluated when steady state had been reached a few hundred orbits later. The planet point mass was placed in the centre of eight cells, where we smoothed the gravitational potential as a usual and necessary technique in planet hydrodynamic simulations. The temperature values within the smoothing length (i.e. what we consider a planet) ranged between 1000 and 4000 K for the different planets, as the radiative module calculated. These values are consistent with the effective temperatures of Jupiter-like planets at the age of 1 Myr of planet interior and evolution models (Mordasini, Marleau & Molliere 2017).

The equation of state in the hydrodynamic simulations was taken to be that of an ideal gas: $P = (\gamma - 1)e$, where $\gamma = 1.43$ adiabatic index connects the pressure P with the internal energy e. The mean molecular weight was 2.3, corresponding to the solar abundances. The viscosity was a constant kinematic viscosity of $10^{-5} a_p{}^2 \Omega_p$, where a_p is the semimajor axis and Ω_p denotes the orbital frequency of the planet.

2.2 RADMC-3D post-processing

To create wavelength-dependent intensity images from the hydrodynamic simulations, we used the RADMC-3D (Dullemond 2012)[1] RT tool. Even though the hydro simulations had a basic RT technique implemented, the results were not wavelength-dependent, because of the use of a Rosseland-mean opacity.

In the near-IR, the scattering of photons on the dust particles is an important mechanism that significantly changes the observability of the CPD and the planet. While this is of particular importance in the optically thin regions (i.e. in the CSD atmosphere), but a large atmosphere cannot be included into the hydrodynamic simulations. It is a known caveat that hydro solvers, especially the Riemann-solver used in our case, fail if the density and energy is too low in a couple of neighbouring cells. The code slows down to a level that the computation basically stalls. Our experience is that below 7.5 deg disc opening angle (that corresponds to roughly 4–5 pressure scale heights) the computations are still safe. To be realistic for the photon scattering, therefore the disc atmosphere had to be extended by extrapolation for the RADMC-3D calculations. In the vertical direction, we fitted Gaussians to the density field, and extrapolated the low-density region so that instead of 40 cells in the colatitude direction we had finally 100. In this region, we kept the temperature as in the last (optically thin) colatitude cells to be sure that the stellar irradiation is still taken account. This means that the temperature in the disc atmosphere was constant with colatitude and higher than the temperature in the bulk of the disc. For the scattering runs, we used 10^7 photons and verified that this value was enough to reach convergence.

To be consistent with the hydrodynamic simulations and the opacity table, we took the RADMC-3D parameters for the star, the dust, and the disc identical to those of the hydrodynamical run. The dust-density files were created from the gas density (which is a good assumption as long as the dust grains are micrometre size and thus are strongly coupled to the gas), by multiplying the gas density in each cell with the dust-to-gas ratio. We assumed thermal equilibrium, hence we used the dust temperature to be equal to the gas temperature, while taking care of the evaporation of the water, silicates, and carbon. Therefore, in the RADMC-3D runs, we used three dust species separated according to their evaporation temperatures:

(i) *Below 170 K:* the dust contains of a mixture of 40 per cent silicate, 40 per cent water, and 20 per cent carbon. The dust density is 1 per cent of the gas density.
(ii) *Between 170 and 1500 K:* water has evaporated, hence the dust contains only silicates and carbon. In these cells, the dust density is 0.6 per cent of the gas density.
(iii) *Between 1500 and 2000 K:* silicates have evaporated, hence the dust contains only carbon. The dust density is 0.2 per cent of the gas density.

Above 2000 K even carbon evaporates, hence in these cells (e.g. very close to the planet) the dust density was set to zero. While in the hydrodynamic simulations the gas opacity was adapted from Bell & Lin (1994), for the RADMC-3D run they cannot be used, as they are mean opacities. Because it would be extremely difficult to obtain the frequency-dependent gas opacities (Malygin et al. 2014), we simply assume that the gas is optically thin in the dust-free zones, even though this is not accurate everywhere.

The RADMC-3D image resolution was set to 1000 × 1000 pixels in each case to avoid resolution problems. The distance of the CSD was assumed to be 100 pc for the calculations of the apparent magnitudes, and for the SEDs.

The SEDs were created with the same initial parameters and data files as the images (including the dust temperature that is calculated by the hydrodynamic code). We ran the `sed` command first for the CSD with using the `fluxcons` command to ensure flux conservation. To determine the CPD SEDs, we ran again the command but with the help of `zoomau` to zoom into the CPD vicinity with a box size of 5 au in each direction from the planet. Due to the high computational cost of the SED runs (making 500 individual image within 1 μm and 10 cm wavelength range), the amount of photons for scattering were set to 'only' 10^4, which already cost a few weeks of core time.

2.3 Flux determination

Given that we would like to provide realistic synthetic images, we choose the parameters of aperture and PSF according to an observation on HD100546 disc (Quanz et al. 2015) taken with the NaCo instrument at the VLT. According to the diffraction limits in these wavelengths, we used for the full width at half-maximum of the Gaussian PSF 56 mas in *Ks* band (2.1 μm), 98 mas in L' band (3.8 μm), and 123 mas in M' band (4.8 μm). The aperture radii were the same as in Quanz et al. (2015). The convolved RADMC-3D synthetic images are shown on Fig. 1. These images do not contain noise, so the presence of the atmosphere is not taken into account, because the noise will depend on the seeing during an actual observation. Because our models have a planet at a known location, it was obvious to determine the flux within one aperture centred on the planet. Given that there is significant contribution of the CSD to the final flux, we also determined the flux at the antiplanet location, i.e. the other side of the CSD with 180 deg shift azimuthally. We then subtracted the flux of this CSD patch from the CPD flux. We also derived the embedded planet flux, as the peak

[1] http://www.ita.uni-heidelberg.de/ dullemond/software/radmc-3d/

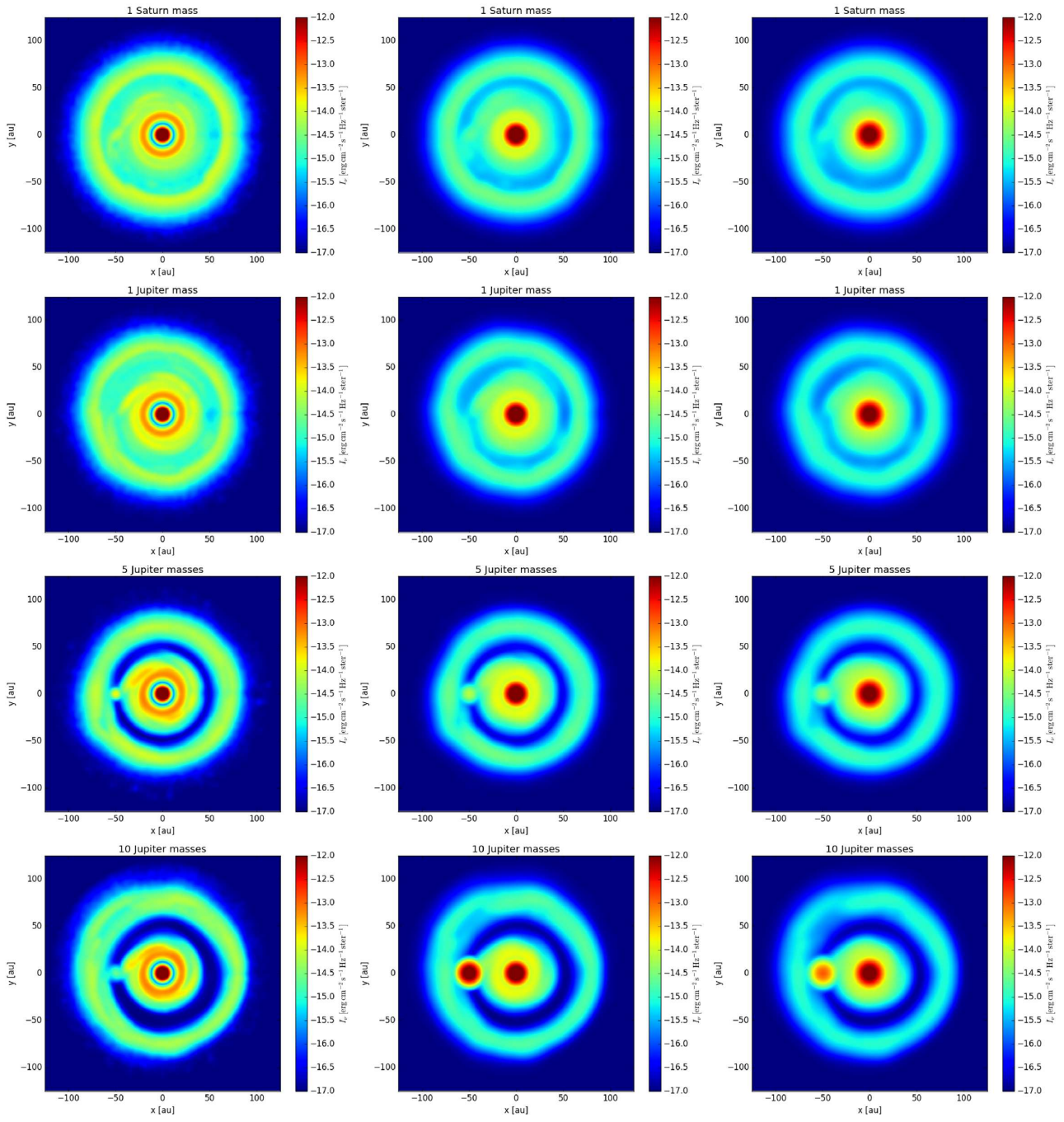

Figure 1. PSF-convolved synthetic images (telescope diameter = 8 m, and distance = 100 pc).

flux within the aperture of the CPD. We converted the fluxes into apparent magnitudes at 100 pc distance. For this, the zero magnitude flux were taken as $F_\nu = 653$ Jy for *Ks*, 253 Jy for L', and 150 Jy for M'.[2]

In the case of CPD, we determined the SED at the planet vicinity using the `radmc3d sed zoomau` commands.

[2]https://www.gemini.edu/sciops/instruments/midir-resources/imaging-calibrations/fluxmagnitude-conversion

3 RESULTS

3.1 SEDs

The hydrodynamic simulations contain an entire ring of the CSD between 20 and 120 au, therefore it is possible to examine the SEDs of this disc. The resulting SEDs are shown in the left-hand panel of Fig. 2. Because the CSD SEDs only have the contribution between 20 and 120 au, they are like transitional discs with a large cavity.

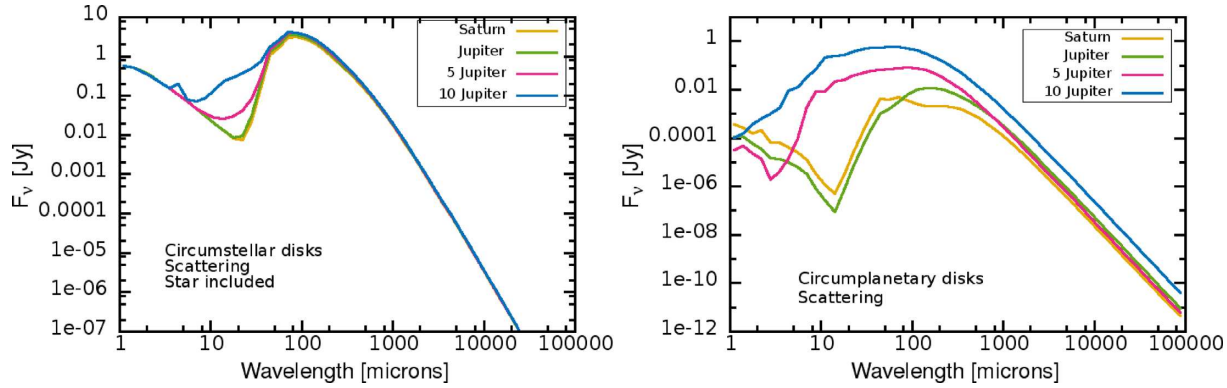

Figure 2. Left: SED of the CSDs (the disc ranges between 20–120 au). Right: SED of the CPDs. Both SEDS are scaled to 100 pc distance.

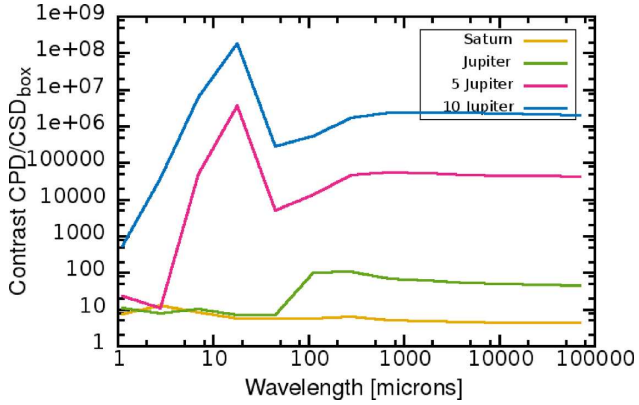

Figure 3. The ratio between the flux of the CPD and the corresponding CSD flux defined in the same sized box (10 au × 10 au) at the 'antiplanet' location (180 deg azimuthally from the planet position) in function of the wavelength. Both SEDs have flux contribution within these boxes laying between 45 and 55 au from the star, because the planets are at 50 au.

On the right-hand panel of Fig. 2, we show the CPD SEDs. Between the different planetary mass simulations, the largest difference of the CPD SEDs is in the 10–100 μm regime, but shorter and longer wavelengths also give some differences. In the near-IR (<5 μm), the difference in flux between the different planetary masses is minimal, and the flux here does not scale with the planetary mass.

Our science goal is to detect the CPD on the background of the CSD, therefore the contrast of their SEDs can inform us which wavelength range is the best to detect the CPD. Since the CPD SEDs were evaluated only in a small area around the planet (in a 10 au × 10 au box, radially between 45 and 55 au from the star, where the planet is at 50 au), we determined the CSD SED within the same sized area as well, 180 deg away from the planet azimuthally. We divided the two box SEDs with each other, to see the contrast between the CPD and CSD SEDs. The resulting contrast informed us about the wavelength range where the difference between the CPD and the CSD is the largest (Fig. 3). For all models, the contrast is poor in the near-IR. For the gap-opening, 5 and 10 M_{Jup} planets the contrast is the best between ~8 and 33 μm (10^7 and 10^9, respectively), so in the vicinity of the 10-μm silicate feature. This is because the CPD is denser than the CSD in the large vicinity of the planet, and in addition, the CSD box is centred at the antiplanet location, i.e. mostly capturing the planetary gap. It is of course easier to spot the CPD in a deep gap, than if the planet would not have opened a gap. The second favourable wavelength range for the highest contrast is beyond 400 μm up until 10 cm, i.e. till the edge of the examined wavelength scale. For the small mass planets, which could not open deep gaps, Fig. 3 shows that a local maximum of the contrast is around 160–200 μm. Beyond this peak, the contrast is roughly constant till 10 cm. The significance of the CPD scales with the planetary mass, the larger is the planetary mass, the easier is to detect the CPD in contrast to the CSD.

Because the SEDs are impacted by the effects of dust scattering and the inclusion of the star, we ran a number of tests to disentangle the different effects on the fluxes at the various wavelengths. We have made SEDs with and without scattering, with and without starlight, and 10 times enhanced dust-to-gas ratio (i.e. 10 × enhanced dust densities) to understand the impacts on the near-IR fluxes, but also to give prediction on all wavelengths between 1 μm to 10 cm. In the following sections, these tests and their results will be described.

3.1.1 *Effects of scattering*

Scattering on dust is an important effect below 10–20 μm. The SEDs show some features (e.g. spikes) at these near-, mid-IR wavelengths, however these spikes are just the result of the Monte Carlo scattering within the RADMC-3D, not molecular/atomic lines. To produce SEDs, one has to limit the amount of photons used in the RT runs in order to have reasonable computational time. When running with the same amount of photons, but different seed number for the Monte Carlo, the flux can change a little. Hence, the spikes should not be taken seriously, or mistaken with gas lines (which were not included in these RT runs). Moreover, we have tested that the reasons for the photon noise lies in the fact that the hot gas dust is very optically thick (>100) in the intermediate vicinity of the planet, hence only few photons can escape even if the calculation is done with 10^7 photons. Simply this fact causes a lot of photon noise, that is inevitable.

Nevertheless, the inclusion of the scattering gives significantly higher fluxes both for the CSD and the CPD (Fig. 4). When not including any star in the model, the scattering gives basically all the flux for the CSD SED below 16 μm for Saturn and 1-Jupiter models (left-hand panel in Fig. 4). The turnover is a bit different at the larger mass planets, it gives most of the flux below 8 μm for the 5 M_{Jup} planet, and below 3 μm for the 10 M_{Jup} case (left-hand panel in Fig. 4). In the case of the CPD SED, scattering contributes

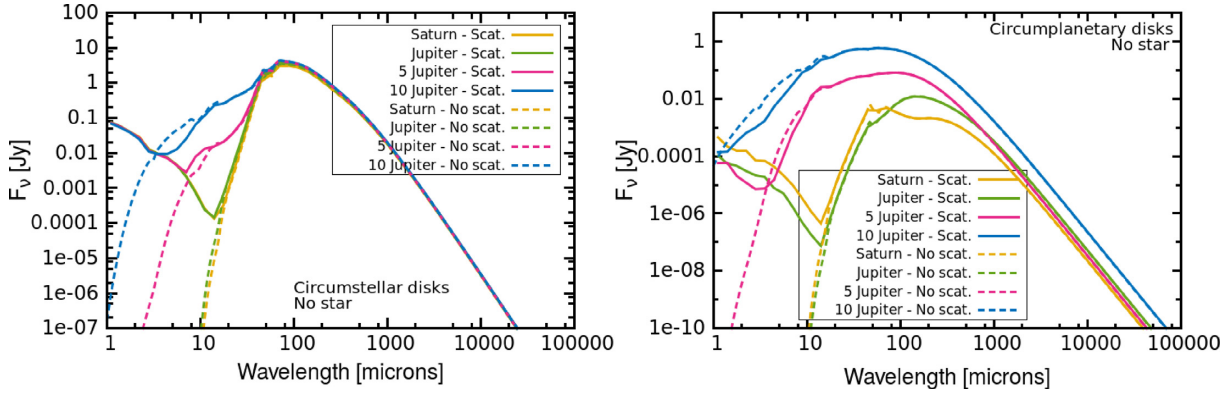

Figure 4. Left: SED of the CSDs with and without scattering; the star is not included. The CSD ranges between 20 au till 120 in these simulations. Right: SED of the CPDs, comparison with and without scattering. Fluxes determined at 100 pc distance.

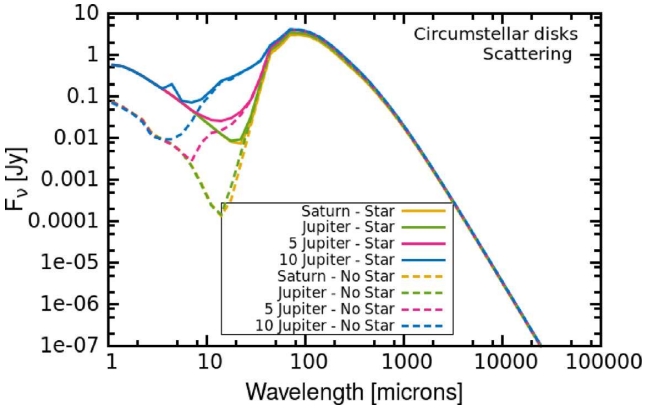

Figure 5. CSD (ranges between 20 and 120 au) SED with scattering, with and without the inclusion of the star. Scaled to 100 pc distance.

basically all the flux below 10 μm, except for the 10 M_{Jup} model, where the no scattering run gives a bit higher flux (right-hand panel in Fig. 4). Beyond 10–20 μm, the fluxes are basically the same with or without scattering.

If we include scattering and compare the same models with and without inclusion of the star, we get of course some difference for the SED of the CSD (Fig. 5). It has larger flux below 25 μm if the star is included (stellar spectrum's Rayleigh–Jeans tail) for Saturn- and Jupiter-models, the other two cases have transition a bit earlier, around 10 μm. Beyond 80 μm, all the SEDs are basically the same, since at this part the stellar irradiation dominates. The inclusion or absence of the star of course does not affect the CPD SED, because the CPD lies far away from the star, the box where the flux was defined does not include the star (and the heating from the planet remains the same and this effect dominates in the CPD).

3.1.2 Effects of enhanced dust-to-gas ratio

To understand how the flux changes with dust disc mass, we enlarged the dust density in every cell by a factor of 10. Hence, both the CSD and the CPD increased its dust mass by a factor of 10. This way the dust-to-gas ratio became 10 per cent instead of 1 per cent.

First, we compare the SEDs of the nominal amount of dust with the enhanced dust, without star and without scattering (i.e. thermal radiation only). For the CSD, it reduces the flux below 10 μm for 5 M_{Jup} and 10 M_{Jup} planet models, for the smaller mass planets it enhances a bit (left-hand panel in Fig. 6). This is due to the difference in gap opening, the two smaller mass planets do not open deep gaps. Beyond 20 μm, it adds flux for all the models (at these wavelengths the CSD is optically thin). The CPD SEDs show similar features (right-hand panel in Fig. 6): in the 5 and 10 M_{Jup} models there is a bit more flux in the near-, mid-IR, while the models with the smaller mass planets remain the same.

When repeating the same exercise (no scattering, with and without enhanced dust density) but adding the star, the result is very similar. The CSD SED is characterized with enhanced flux beyond ∼20 μm when the dust density is 10 × the nominal one (left in Fig. 7). Between 5 and 20 μm, it usually results in less flux when adding more dust to the models. Below ∼5 μm, the flux is the same. The CPD SED contains a little more flux in the near-, mid-IR for the two large mass planet cases (right in Fig. 7), the smaller mass planet models are roughly the same irrespective of the enhanced dust-to-gas ratio in the CPDs.

When one includes scattering for the 10x dust density models, and compares them with the nominal models with scattering the results are somewhat unexpected. In this case, there is no star included for clarity (Fig. 8). The CSD SED has less flux below 25–40 μm (depending on the planet mass) if the dust density is 10x higher, however, there is always more flux beyond 50 μm with increased dust density (left panel in Fig. 8). The CPD SEDs are quite noisy in the near-IR due the photon noise, but for the Saturn-, Jupiter-mass, and 5 Jupiter-mass planet models the inclusion of more dust reduces the flux below ∼10 μm, while one can expect the opposite for the 10M_{Jup} planet in this wavelength region (right-hand panel in Fig. 8). Beyond 200 μm, the 10x dust gives higher fluxes for all models. In all wavelengths, the difference between the nominal and 10x dust mass models are very small.

3.2 Near-IR fluxes

In Table 1, we summarize the fluxes and magnitudes of the embedded planet and the CPD+planet from our simulations in *Ks*, *L*′, and *M*′ bands. The CSD contribution to the CPD fluxes was already subtracted. Fig. 9 shows visually the fluxes for each given band, and in comparison to theoretical models of Baraffe et al. (2003) and Spiegel & Burrows (2013). The CPD as a whole is brighter than the planet itself, which is also a consequence on how we determined

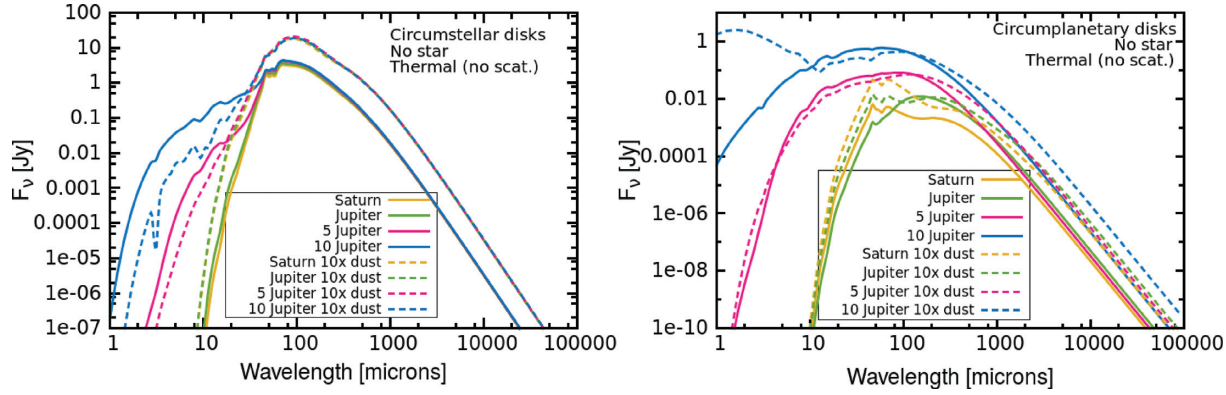

Figure 6. Left: SED of the CSDs (ranges between 20 and 120 au) with and without 10x enhanced dust mass (dust-to-gas ratio of 10 per cent). There is no star, nor scattering included in this SED. Right: corresponding SED of the CPDs. Distance is 100 pc.

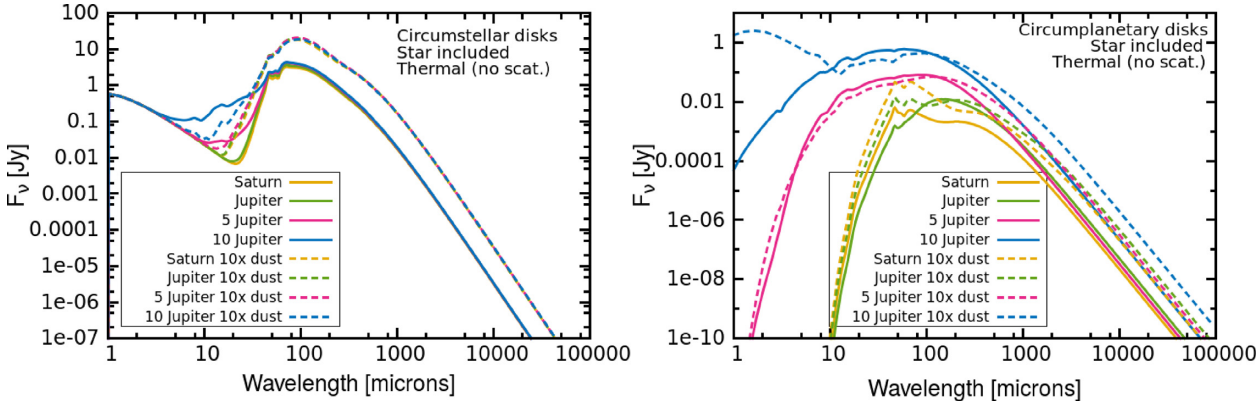

Figure 7. Left: SED of the CSDs (ranges between 20 and 120 au) with and without 10x enhanced dust mass (dust-to-gas ratio of 10 per cent). The star is included, but scattering is not. Right: corresponding SED of the CPDs. Scaled to 100 pc distance.

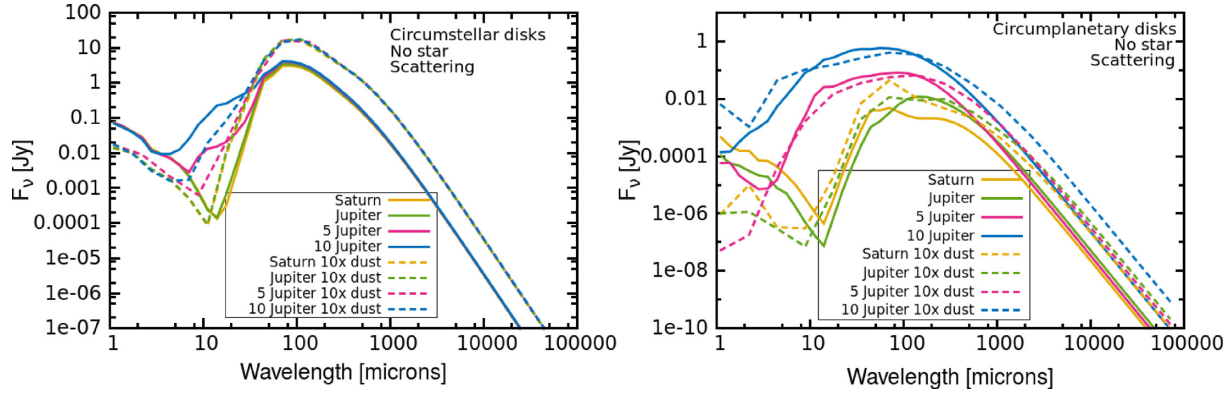

Figure 8. Left: SED of the CSDs (ranges between 20 and 120 au) with and without 10x enhanced dust mass (dust-to-gas ratio of 10 per cent). The star is included, as well as scattering. Right: corresponding SED of the CPDs. Fluxes shown at 100 pc distance for both SEDs.

their fluxes: for the CPD, we integrated the flux of the pixels within one aperture and for the planet we only refer as a peak value within this region. Nevertheless, from the CPD aperture flux we subtracted the circumstellar contribution by defining the flux at the antiplanet location (i.e. 180 deg away from the planet azimuthally) within one aperture as well. The ratio between the CPD flux (without the subtraction of the CSD flux) and the flux at the antiplanet location within one aperture is the SNR_{CPD} listed in the Table 1. This helps determining how significant is the CPD signal in comparison to the underlying CSD. This contrast is at least two orders of magnitude larger for the 5 and 10 M_{Jup} planet models, than in the lower planetary masses (last column in Table 1). In fact, when one visually inspects the synthetic images on Fig. 1, the presence of the planet is not obvious for the Saturn and Jupiter cases, in these cases the detection of the hotspot due to the planet+CPD would be very unlikely.

Table 1. Embedded planet and CPD fluxes and magnitudes at 100 pc.

M_P (M_{Jup})	Band	$Flux_P$ (Jy)	$Flux_{CPD}$ (Jy)	Mag_P (mag)	Mag_{CPD} (mag)	SNR_{CPD}†
10.0	*Ks*	4.22e–16	8.14e–06	27.56	19.76	227.81
10.0	*L′*	7.84e–13	1.55e–03	18.35	13.03	10149.32
10.0	*M′*	2.73e–12	5.38e–03	16.43	11.11	7528.27
5.0	*Ks*	3.00e–13	1.48e–04	20.43	16.61	1079.38
5.0	*L′*	8.70e–14	1.78e–04	20.74	15.38	141.01
5.0	*M′*	8.11e–14	1.70e–04	20.25	14.87	48.61
1.0	*Ks*	1.03e–15	1.57e–05	26.58	19.05	3.65
1.0	*L′*	4.38e–16	2.87e–05	26.49	17.36	3.78
1.0	*M′*	2.61e–16	3.00e–05	26.48	16.75	2.79
0.3	*Ks*	7.71e–15	9.10e–05	24.40	17.14	13.85
0.3	*L′*	2.72e–15	6.69e–05	24.50	16.44	4.92
0.3	*M'*	1.64e–15	4.85e–05	24.49	16.23	3.01

Notes. †SNR_{CPD} is defined as the flux ratio between the CPD flux within the aperture versus the flux of the CSD within the same sized aperture 180 degr away from the planet, i.e. at the 'antiplanet' location.

In comparison to the theoretical models of Baraffe and Spiegel and Burrows, it is clear that the embedded planets in our simulations are fainter, because the extinction due to the CPD is significant. It is just a coincidence that some of the CPD magnitudes fit well to the planet brightness predictions of these evolutionary models. We did not try to match the luminosity of the planets in our simulations with either of the above planet evolution model prediction, because the planet luminosity in the formation phase is unknown. The evolutionary models either way do not include the hot-bath of the CPD in this evolutionary phase, their planets are always considered to be detached from their parent disc. To access the CPD/planet brightness ratio, therefore, we compare the planet and the CPD both from our simulations for consistency.

In Fig. 9, one can see that the embedded planet and CPD magnitudes do not scale with the planetary mass. This is due to the fact that the scattering is important in this wavelength range. If one would consider purely the thermal (i.e. without scattering) fluxes, both the CPD and the planet fluxes would be ordered according to the planet masses, i.e. the higher mass planet has brighter CPD, as can be seen in the SEDs in the right-hand panel of Fig. 8. As it was described in Section 3.1.1, the Monte Carlo scattering within the RADMC-3D runs can result in different fluxes on the CPDs, depending on what was the seed number, or how many photons were used. Hence, to get robust results on the *Ks*, *L′*, and *M′* magnitudes, we run the same RADMC-3D runs 10 times with 10^7 photons in each case, then took the median value in each pixel of the 10 images, and calculated the brightness values in this final image. Hence the reported brightnesses are robust, the fact that the near-IR fluxes does not scale with planetary mass is not the effect of the Monte Carlo noise.

The observability of the planet+CPD is strongly dependent on the planetary gap depths in the near-IR as well. Fig. 1 shows that the gaps are clearer and deeper towards the longer wavelengths, making it easier to separate the CPD from the CSD. Of course, the more massive is the planet, the deeper and wider gap it creates within the CSD, hence observing larger mass planets is always easier.

We have run several tests to understand the robustness of the fluxes. First, we tested the number of photons used in the RADMC-3D runs, whether the fluxes we determined above are converged. In case one uses too low amount of photons, the fluxes can change significantly. Therefore, instead of 10^7 photons used for scattering in the nominal models, we also run a suite of RT modelling with an order of less photons, i.e. only 10^6 photons for the Saturn-mass planet model. The error on the intensities were within 0.06 per cent, 0.01 per cent, and 0.04 per cent for *Ks*, *L′*, and *M′* bands, respectively. Moreover the brightness of the CPD will depend on the dust albedo and on the optical thickness of the CPD. We describe the findings on the planet and CPD magnitudes in Section 3.3 in order to address the issue of the planetary mass estimation from the observed brightnesses.

3.3 Planetary mass overestimation

In Section 3.2, it was mentioned that the CPD flux is significantly larger than that of the planet. It is worthwhile to quantify this difference at the various bands, in order to give an estimate about how much the planetary mass from the observed flux can be overestimated, by assuming that the detected flux solely comes from the planet, and not from the CPD. In Fig. 11 we show the difference between the CPD magnitude and the embedded planet from our models. For the barely gap-opening planets (i.e. Saturn and Jupiter), all three bands are giving roughly the same difference of ∼7.8 and ∼8.6 mag, respectively. This large difference can lead to a factor of 100 overestimation of the planet mass according to the Baraffe-models (assuming an age of 1 Myr). For the larger mass planet cases (5 and 10 M_{Jup}) in *L′* and *M′* bands, the difference is 5.3 mag, which translates to a factor of 20 overestimation of mass using the Baraffe-models.

The brightness of the CPD will depend on the dust albedo and on the optical thickness of the CPD and hence its mass. In near-IR most of the flux is coming from the photon scattering on dust particles, hence the amount of dust in the CPD will matter for the magnitudes. Because the CPD is continuously fed by the CSD, its mass mostly changes together with that of the CSD (Szulágyi 2017). Therefore, we tested the fluxes when the dust density was increased by a factor of 10 in every cell of the models (i.e. both the CSD and the CPD mass was increased by an order of magnitude). We found that the CPD magnitude does not linearly scale with dust mass. The CPD brightness at 100 pc will be 3.8 mag fainter for the Saturn- and Jupiter-mass planet models if the dust density is increased by 10. On the contrary, for the higher mass planets the brightness will increase, for the 5 Jupiter-mass case by 7.6 mag, for the 10 M_{Jup} case by 1.5 mag on average for the bands *Ks*, *L′*, and *M′*. This shows that the CPD brightness in near-IR will strongly depend on the dust

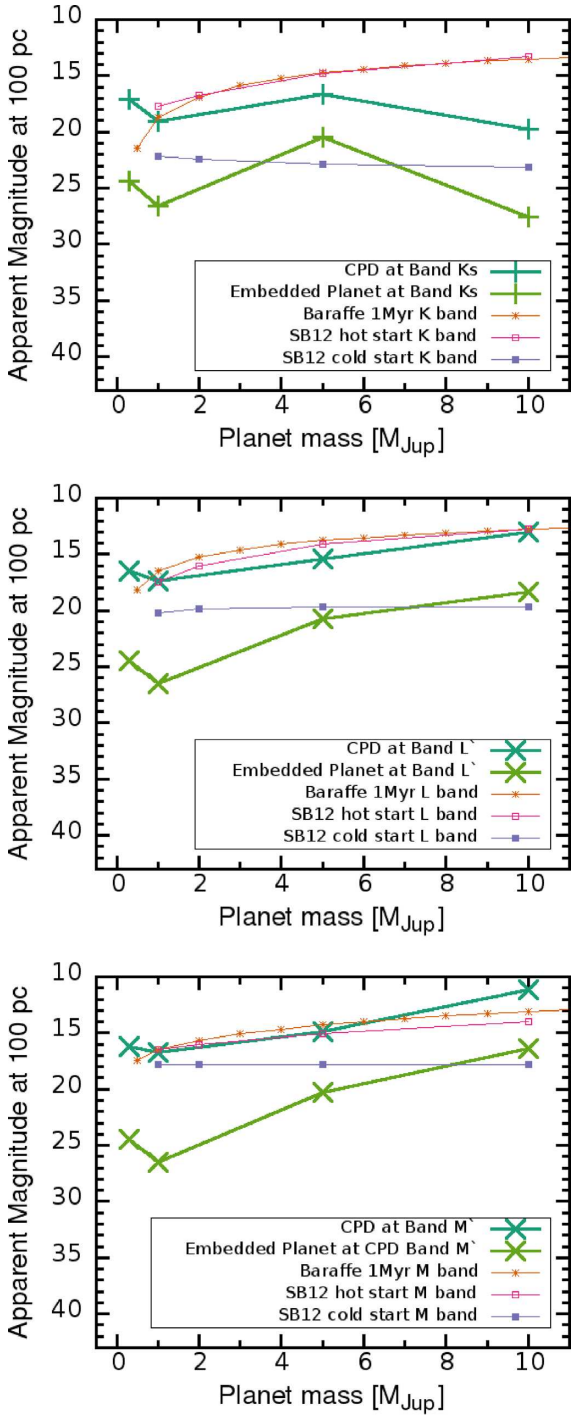

Figure 9. Apparent magnitudes of *Ks*, L', and M' bands of the embedded planet and the CPD+planet.

mass, and whether or not there is a deep gas gap around the CPD (i.e. the amount of extinction).

Our tests have revealed, that no matter what model we use, the CPD brightness will be larger than that of the planet's by several magnitudes. The CPD brightness will depend on the disc parameters, e.g. its the dust-to-gas ratio. Hence, when trying to estimate the forming planet mass based on near-IR observations, the planet evolutionary models cannot be used. These models can be useful when there is no more gaseous CPD around the planet, i.e. when there is no more gaseous CSD in the system.

4 DISCUSSION

Like every model and simulation, ours also have several limitations. First of all, in this work we used the assumption of a fixed dust-to-gas ratio of 0.01. It is known since a long while that CSDs can have dust traps where locally the dust-to-gas ratio is enhanced (e.g. Youdin & Goodman 2005; Birnstiel, Klahr & Ercolano 2012; Meheut et al. 2012; van der Marel et al. 2013; Drążerrorzdotkowska & Dullemond 2014), but recently such traps has been found even in CPDs (Drazkowska & Szulágyi 2018). Even considering the bulk dust-to-gas ratio of the discs globally, different systems show very different values between 0.1 and 0.001 for CSDs (e.g. Williams & Best 2014; Ansdell et al. 2016). In Section 3.1.2, we ran tests about if the dust-to-gas ratio is larger than 1 per cent. We expect, that if the ratio would be smaller than 1 per cent, then we would find the opposite behaviour as described in Section 3.1.2. Beyond 20–50 μm, there would be less flux in the SEDs than our nominal 1 per cent case, and more in flux in the shorter wavelengths.

The semimajor axes of the planets will also play a major role on the CPD brightness. The further away the planet lies from the star, its CPD will be colder just as a tumbs of rule. As the gas density is smaller in the outer CSD, the CPD will get optically thinner, hence its cooling time will enhance rapidly. On the other hand, if the CPD is optically thick (e.g. lies close to the star in the optically thick part of thr CSD, or when the CSD is massive), then it will be significantly hotter, hence brighter. Even though we have 5 au simulations at hand, with the same aperture sizes it would have been impossible to measure the CPD and planet magnitudes.

Our hydrodynamic simulations are disc simulations, without proper treatment for the planet. Our approach was to fix the radius and mass of the gas giants, but in the formation phase these are highly unknown parameters. These values affect the planet brightness the most, hence with different setup our embedded planet fluxes could change as well. If the mass of the CSD is larger, the accretion rate to the planet will also increase (Szulágyi, Mayer & Quinn 2016b). The enhanced accretion rate in turn will increase the CPD brightness through the accretional luminosity (Zhu 2015; Szulágyi et al. 2016a). In our previous work of Szulágyi & Mordasini (2016), we estimated the accretion luminosity of planets with orbital separation of 5.2 au. They all turned out to be on the order of a few times $10^{-5}L_{Sun}$. We also calculated the accretional luminosities for the 50 au separation planets presented in this work. The accretion luminosities are a few times $10^{-6}L_{Sun}$, so smaller than the close-in planet's. In comparison, the Baraffe-model's planet luminosities at age of 1 Myr for a Jupiter-mass giant is almost $10^{-5}L_{Sun}$ and for a 10 Jupiter-mass planet is $10^{-3}L_{Sun}$. If these estimations are correct, the accretion luminosities of the planets (not the CPD accretion rate and the corresponding luminosity) are slightly smaller than the intrinsic planet luminosities. Note, that the planet accretion rate, and the corresponding accretional luminosity is smaller than the CPD accretion rate and the corresponding accretion luminosity. The accretion to the CPD is $\sim$ an order of magnitude higher than to the planet, and henceforth the accretion luminosity ($GM_{planet}\dot{M}_{planet}/R_{planet}$) of the CPD is also higher than that of the planet's. Due to the meridional circulation and that the CPD is a deaccreting disc, most of the gas entering the CPD will not end up in the planet, but will be reprocessed into the CSD (Szulágyi et al. 2014; Fung & Chiang 2016).

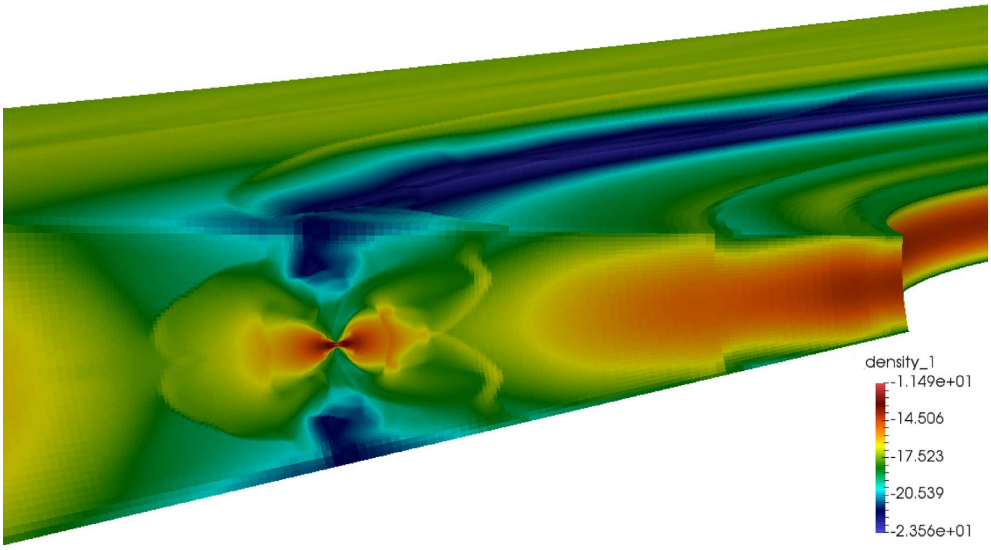

Figure 10. The gas density from one of the hydrodynamic simulations in order to show how much the planet is embedded. The small disc with the orange colour is the CPD, and the planet can be seen in the middle of that disc. The green colours show that there is significant amount of dust and gas density above the planet, even though the planet opened a gap, hence the extinction of the planet brightness is strong.

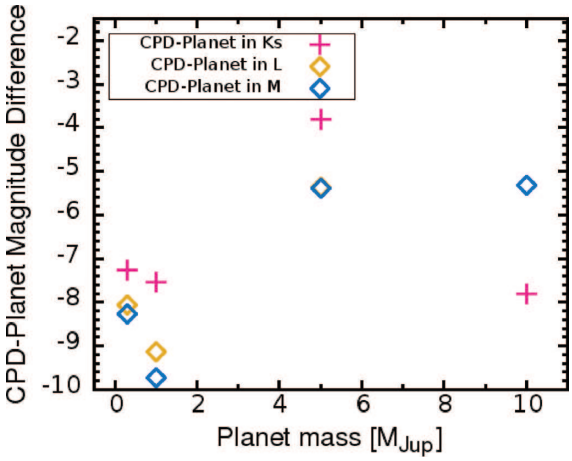

Figure 11. The magnitude difference between the CPD and the embedded planet in our models at the *Ks*, L', and M' bands.

Our work was not including hydrogen dissociation and ionization. This can have an effect on the temperatures and on the calculated magnitudes. If the energy would go into dissociating and ionizing hydrogen, the temperatures could be lower. However, the area in the simulation where the temperature would go as high to dissociate or ionize hydrogen, is extremely small, only few cells in these simulations. In comparison, when the planet was placed at 5.2 au from the star, and therefore the CPD was in an optically thick and hotter part of the CSD, the dissociation and ionization only affected the very vicinity of the planet, inside of the planet and the hottest part of the shock front on the CPD surface (fig. 3 in Szulágyi & Mordasini 2016).

Moreover, we neglected magnetic fields. This can change the accretion flow and rate to the CPD and to the planet (Gressel et al. 2013; Keith & Wardle 2015; Owen & Menou 2016), that could change our conclusions. Self-gravity was also neglected due to the small mass of CPDs. However, in heavy CSDs, maybe the CPDs could also become gravitationally unstable (Lubow & Martin 2012).

As we showed it in Sections 3.1.2 and 3.3, the dust mass of the CPD and the semimajor axis of the planet will affect the brightness of the planet and its CPD in all wavelength hence to determine the CPD brightness one should perform system-specific modelling. In addition, in this work we only considered one initial CSD mass and viscosity, we could not explore the parameter space further with these complex simulations.

5 CONCLUSIONS

We performed a study on the CPD brightness by creating their SEDs and by examine their near-IR (*Ks*, M', and L') fluxes with synthetic images. We ran radiative hydrodynamic simulations of Saturn, Jupiter, 5 Jupiter-, and 10 Jupiter-mass planets placed at 50 au from their star still embedded in their natal CSDs. In this phase, these planets are surrounded by a CPD, which we examined in high resolution placing nested meshes in the planet vicinity. We then post-processed these hydrodynamic simulations with RADMC-3D RT tool to create wavelength-specific images and SEDs. For the dust, we assumed a constant 1 per cent dust-to-gas ratio with a composition of 40 per cent silicate, 40 per cent water, and 20 per cent carbon and we took care of the evaporation of these species if the temperatures were high enough in a given cell.

Our finding is that the best contrast ratio between the CPD with the surrounding CSD is between ∼8 and 33 μm if the planets opened deep gaps (i.e. $\geq 5 M_{\rm Jup}$), and this contrast is particularly poor in the near-IR. For all planetary masses, the sub-mm/radio wavelengths provide also good contrast with the CSD, so this wavelength range provide unprecedented opportunity to detect forming planets and their CPDs, similarly as previous studies pointed also out (Isella & Turner 2016; Szulágyi et al. 2018). The CPD SEDs revealed that the CPD brightness below ∼10 μm is dominated by the scattering of photons on the dust of this disc. In conclusion, to separate the CPD from the CSD observationally, the best chance is targeting

sub-mm/radio wavelengths or in case of massive planets ($\geq 5M_{Jup}$) the 10-μm silicate feature vicinity.

We also pointed out that the CPD brightness is always higher than that of the embedded planet, which could easily lead to a planet-mass overestimation by an order of magnitude. Hence, when trying to estimate the forming planet mass from the detected brightness, the planet evolutionary models cannot be used. In the formation phase, we cannot detect the planets directly, only their CPD. But the CPD magnitude will depend mainly on the disc parameters, e.g. the dust-to-gas ratio of the CPD, the distance from the star (CPDs closer to the star are hotter and brighter), viscosity etc. We found that the CPD brightness does not scale linearly with the dust mass, and will strongly depend on whether the planet opened a deep gas gap ($\geq 5M_{Jup}$) or not ($\leq 1M_{Jup}$) because of extinction. Our recommendation is to run system-specific disc modelling if one is trying to estimate the planetary mass in the formation phase from the observed brightness.

ACKNOWLEDGEMENTS

This work has been in part carried out within the Swiss National Science Foundation (SNSF) Ambizione grant PZ00P2_174115. SPQ acknowledges the funding from the National Centre for Competence in Research 'PlanetS' supported by the Swiss National Science Foundation. Computations have been done on the 'Mönch' machine hosted at the Swiss National Computational Centre.

REFERENCES

Ansdell M. et al., 2016, ApJ, 828, 46
Ayliffe B. A., Bate M. R., 2009, MNRAS, 397, 657
Ayliffe B. A., Bate M. R., 2012, MNRAS, 427, 2597
Baraffe I., Chabrier G., Barman T. S., Allard F., Hauschildt P. H., 2003, A&A, 402, 701
Bell K. R., Lin D. N. C., 1994, ApJ, 427, 987
Birnstiel T., Klahr H., Ercolano B., 2012, A&A, 539, A148
Bitsch B., Morbidelli A., Lega E., Crida A., 2014, A&A, 564, A135
Bohren C. F., Huffman D. R., 1984, Nature, 307, 575
Borra E. F., Deschatelets D., 2018, MNRAS, 481, 4841
Brittain S. D., Carr J. S., Najita J. R., Quanz S. P., Meyer M. R., 2014, ApJ, 791, 136
Brunngräber R., Wolf S., 2018, A&A, 611, A90
Commerçon B., Teyssier R., Audit E., Hennebelle P., Chabrier G., 2011, A&A, 529, A35
Currie T. et al., 2014, ApJ, 796, L30
Davies R. et al., 2018, SPIE1, 10702, 1070209
de Val-Borro M. et al., 2006, MNRAS, 370, 529
Draine B. T., 2003, ApJ, 598, 1026
Drazkowska J., Szulágyi J., 2018, ApJ, 866, 142
Drazkowska J., Dullemond C. P., 2014, A&A, 572, A78
Dullemond C. P., 2012, Astrophysics Source Code Library, record ascl:1202.015
Eisner J. A., 2015, ApJ, 803, L4
Follette K. B. et al., 2017, AJ, 153, 264
Fung J., Chiang E., 2016, ApJ, 832, 105
Gressel O., Nelson R. P., Turner N. J., Ziegler U., 2013, ApJ, 779, 59
Isella A., Turner N., 2018, APJ, 860, 27
Keith S. L., Wardle M., 2015, MNRAS, 451, 1104
Keppler M. et al., 2018, A&A, 617, A44
Kley W., 1999, MNRAS, 303, 696
Kraus A. L., Ireland M. J., 2012, ApJ, 745, 5
Lubow S. H., D'Angelo G., 2006, ApJ, 641, 526
Lubow S. H., Seibert M., Artymowicz P., 1999, ApJ, 526, 1001
Lubow S. H., Martin R. G., 2012, ApJ, 749, L37
Malygin M. G., Kuiper R., Klahr H., Dullemond C. P., Henning T., 2014, A&A, 568, A91
Meheut H., Meliani Z., Varniere P., Benz W., 2012, A&A, 545, A134
Mordasini C., Marleau G.-D., Molliere P., 2017, A&A, 608, A72
Osorio M. et al., 2014, ApJ, 791, L36
Owen J. E., Menou K., 2016, ApJ, 819, L14
Quanz S. P., Amara A., Meyer M. R., Girard J. H., Kenworthy M. A., Kasper M., 2015, ApJ, 807, 64
Quillen A. C., Trilling D. E., 1998, ApJ, 508, 707
Rameau J. et al., 2017, AJ, 153, 244
Reggiani M. et al., 2014, ApJ, 792, L23
Reggiani M. et al., 2017, A&A, 611, A74,
Sallum S. et al., 2015, Nature, 527, 342
Spiegel D. S., Burrows A., 2013, ApJ, 776, 138
Szulágyi J., Morbidelli A., Crida A., Masset F., 2014, ApJ, 782, 65
Szulágyi J., Masset F., Lega E., Crida A., Morbidelli A., Guillot T., 2016, MNRAS, 460, 2853
Szulágyi J., Mayer L., Quinn T., 2017, MNRAS, 464, 3158
Szulágyi J., Mordasini C., 2017, MNRAS, 465, L64
Szulágyi J., van der Plas G., Meyer M. R., Pohl A., Quanz S. P., Mayer L., Daemgen S., Tamburello V., 2018, MNRAS, 473, 3573
Szulágyi J., 2017, ApJ, 842, 103
van der Marel N. et al., 2013, Science, 340, 1199
Warren S. G., Brandt R. E., 2008, J. Geophys. Res., 113, D14220
Williams J. P., Best W. M. J., 2014, ApJ, 788, 59
Youdin A. N., Goodman J., 2005, ApJ, 620, 459
Zhu Z., 2015, ApJ, 799, 16
Zubko V. G., Mennella V., Colangeli L., Bussoletti E., 1996, MNRAS, 282, 1321

This paper has been typeset from a TEX/LATEX file prepared by the author.